Structural and functional basis of the selectivity filter as a gate in human TRPM2 channel

Graphical abstract
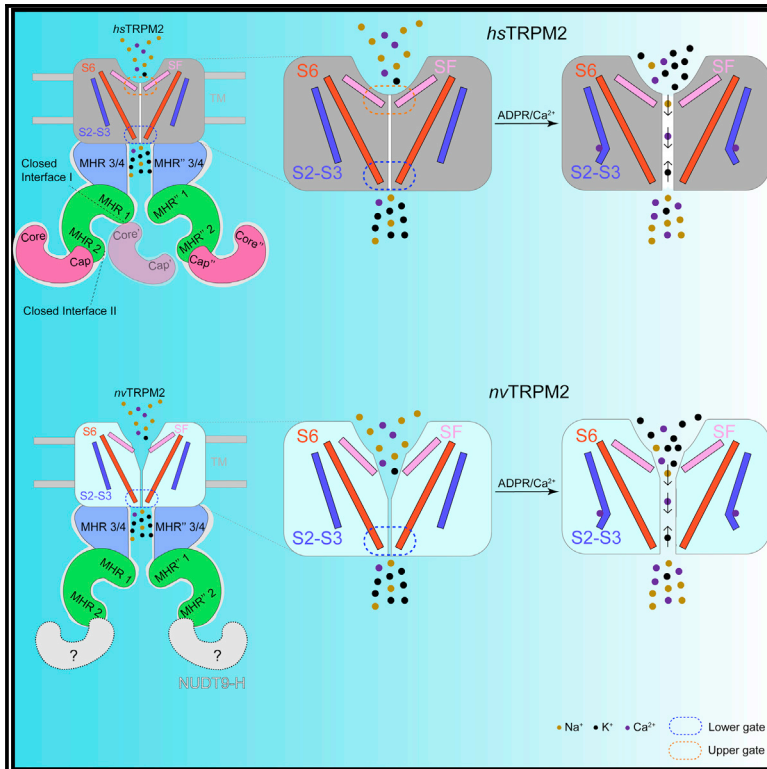
Authors

Xiafei Yu, Yuan Xie, Xiaokang Zhang, ...,
Fan Yang, Jiangtao Guo, Wei Yang

Correspondence

fanyanga@zju.edu.cn (F.Y.),
jiangtaoguo@zju.edu.cn (J.G.),
yangwei@zju.edu.cn (W.Y.)

In brief

Yu et al. report the apo state of the human TRPM2 (*hs*TRPM2) structure in nanodisc. Cryo-EM-guided modeling and patch-clamp recording further identify a quadruple-residue motif (^{979}FGQI^{982}) as both the selectivity filter and a gate. In contrast, the selectivity filter of the *Nematostella vectensis* TRPM2 (*nv*TRPM2) does not form a gate.

Highlights

- A more physiologically relevant *hs*TRPM2 apo structure is determined in nanodisc

- The ^{979}FGQI^{982} motif in the pore is identified as the ion selectivity filter in *hs*TRPM2

- The selectivity filter of *hs*TRPM2 acts as a gate to control ion permeation

- The selectivity filter of *nv*TRPM2 does not serve as a gate

Cell Reports

Article

Structural and functional basis of the selectivity filter as a gate in human TRPM2 channel

Xiafei Yu,[1,13] Yuan Xie,[2,13] Xiaokang Zhang,[3,4,5,13] Cheng Ma,[6,13] Likun Liu,[1] Wenxuan Zhen,[7] Lingyi Xu,[2] Jianmin Zhang,[1] Yan Liang,[8] Lixia Zhao,[9] Xiuxia Gao,[9] Peilin Yu,[8] Jianhong Luo,[10] Lin-Hua Jiang,[11,12] Yan Nie,[10] Fan Yang,[7,*] Jiangtao Guo,[2,*] and Wei Yang[1,14,*]

[1]Departments of Biophysics and Neurosurgery, The First Affiliated Hospital, Zhejiang University School of Medicine, Hangzhou, Zhejiang 310058, P. R. China
[2]Departments of Biophysics and Pathology of Sir Run 14, Shaw Hospital, Zhejiang University School of Medicine, Hangzhou 310058, P. R. China
[3]Center of Cryo-Electron Microscopy, Zhejiang University School of Medicine, Hangzhou 310058, P. R. China
[4]Interdisciplinary Center for Brain Information, The Brain Cognition and Brain Disease Institute, Faculty of Life and Health Sciences, Shenzhen Institute of Advanced Technology, Chinese Academy of Sciences, Shenzhen, Guangdong 518055, China
[5]Shenzhen-Hong Kong Institute of Brain Science-Shenzhen Fundamental Research Institutions, Shenzhen, Guangdong 518055, China
[6]Co-facility center, Zhejiang University School of Medicine, Hangzhou, Zhejiang 310058, P. R. China
[7]Department of Biophysics and Kidney Disease Center, The First Affiliated Hospital, Zhejiang University School of Medicine, Hangzhou, Zhejiang 310058, P. R. China
[8]Departments of Toxicology and Medical Oncology of Second Affiliated Hospital, Zhejiang University School of Medicine, Hangzhou, Zhejiang 310058, P. R. China
[9]Shanghai Institute for Advanced Immunochemical Studies, ShanghaiTech University, Shanghai 201210, P. R. China
[10]Department of Neurobiology, Key Laboratory of Medical Neurobiology of the Ministry of Health of China, Zhejiang Province Key Laboratory of Neurobiology, Zhejiang University School of Medicine, Hangzhou, Zhejiang 310058, P. R. China
[11]School of Biomedical Sciences, Faculty of Biological Sciences, University of Leeds, Leeds LS2 9JT, UK
[12]Sino-UK Joint Laboratory of Brain Function and Injury, Department of Physiology and Neurobiology, Xinxiang Medical University, Xinxiang, P. R. China
[13]These authors contributed equally
[14]Lead contact
*Correspondence: fanyanga@zju.edu.cn (F.Y.), jiangtaoguo@zju.edu.cn (J.G.), yangwei@zju.edu.cn (W.Y.)
https://doi.org/10.1016/j.celrep.2021.110025

SUMMARY

Transient receptor potential melastatin 2 (TRPM2), a Ca^{2+}-permeable cation channel, is gated by intracellular adenosine diphosphate ribose (ADPR), Ca^{2+}, warm temperature, and oxidative stress. It is critically involved in physiological and pathological processes ranging from inflammation to stroke to neurodegeneration. At present, the channel's gating and ion permeation mechanisms, such as the location and identity of the selectivity filter, remain ambiguous. Here, we report the cryo-electron microscopy (cryo-EM) structure of human TRPM2 in nanodisc in the ligand-free state. Cryo-EM map-guided computational modeling and patch-clamp recording further identify a quadruple-residue motif as the ion selectivity filter, which adopts a restrictive conformation in the closed state and acts as a gate, profoundly contrasting with its widely open conformation in the *Nematostella vectensis* TRPM2. Our study reveals the gating of human TRPM2 by the filter and demonstrates the feasibility of using cryo-EM in conjunction with computational modeling and functional studies to garner structural information for intrinsically dynamic but functionally important domains.

INTRODUCTION

Oxidative stress, arising from excessive generation of reactive oxygen species (ROS) and/or impairment in antioxidant defense and strongly implicated in the pathogenesis of a number of diseases, is linked to ion homeostasis and intracellular signaling pathways by regulating ion channel activity (Coyle and Puttfarcken, 1993; Kietzmann et al., 2000). Transient receptor potential (TRP) melastatin 2 (TRPM2) channel, a Ca^{2+}-permeable non-selective cation channel belonging to

the tetrameric TRP channel superfamily, is often referred to as a ROS sensor in diverse cell types, such as neurons, pancreatic β cells, endothelial cells, macrophages, microglia, and pericytes (Alawieyah Syed Mortadza et al., 2018; Dietrich and Gudermann, 2008; Hara et al., 2002; Jiang et al., 2010, 2017; Kashio et al., 2012; Nagamine et al., 1998; Uchida and Tominaga, 2011; Ye et al., 2014). Accumulating evidence supports a crucial role for TRPM2 in multiple physiological functions, such as warmth sensation, insulin secretion, and immune responses, and in numerous oxidative stress-related
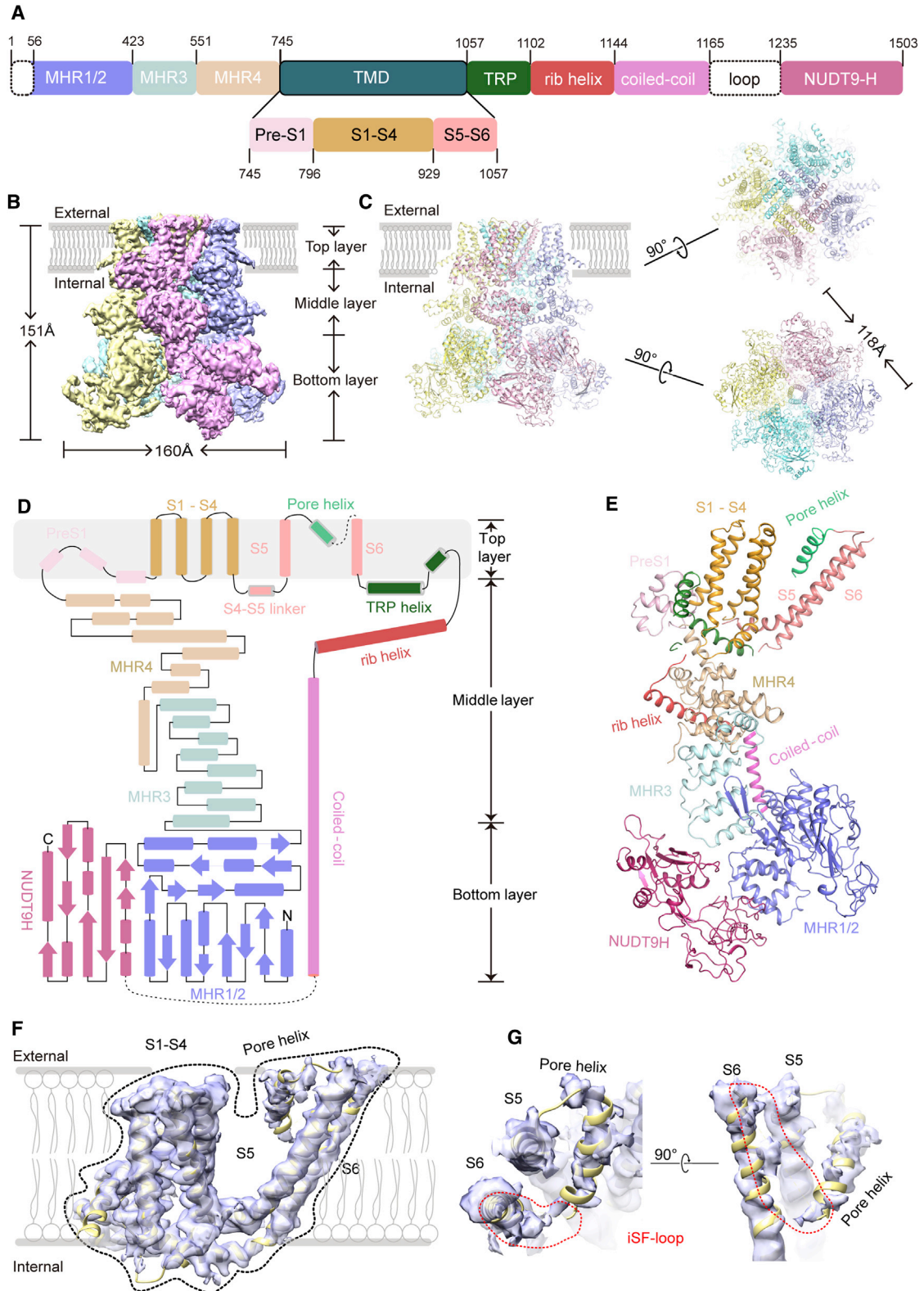
(legend on next page)

pathologies, including diabetes, chronic pain, stroke, Alzheimer's disease, and depression (Julius, 2013; Ko et al., 2019; Miller et al., 2014; Ostapchenko et al., 2015; Uchida and Tominaga, 2011). Therefore, TRPM2 is highly attractive as a potential target for oxidative stress-related diseases.

As one of the NAD$^+$ metabolites, adenosine diphosphate ribose (ADPR) is a molecule critically involved in oxidative stress (Blenn et al., 2011). ADPR and Ca^{2+} are required for activation of mammalian TRPM2 channels. Previous functional studies suggest that ADPR binds to the TRPM2-specific NUDT9-H domain in the distal C terminus (Perraud et al., 2001, 2003), which is supported by subsequent mutagenesis studies that identify several residues crucial for ADPR-induced channel activation (Fliegert et al., 2017; Kühn and Lückhoff, 2004; Yu et al., 2017). There is also functional evidence to suggest that an IQ-like calmodulin-binding motif and an EF-hand in the N terminus are involved in Ca^{2+}-induced TRPM2 channel activation (Du et al., 2009; Luo et al., 2018; Tong et al., 2006). Recent cryo-electron microscopy (cryo-EM) studies have reported structures of human (hs) TRPM2, as well as non-mammalian *Nematostella vectensis* (nv) and *Danio rerio* (dr) TRPM2 channels, in ligand-free state, ADPR-bound state, Ca^{2+}-bound state, and ADPR/Ca^{2+}-bound state (Huang et al., 2018, 2019; Wang et al., 2018; Yin et al., 2019; Zhang et al., 2018). These structures demonstrate two ADPR binding sites in human TRPM2 (hsTRPM2), one in the N-terminal MHR1/2 domain and the other in the C-terminal NUDT9-H domain. In addition, one Ca^{2+} binding site in the intracellular S2-S3 loop is revealed and proposed to mediate Ca^{2+} binding that induces conformational changes leading the ADPR-bound closed channel to open (Huang et al., 2018, 2019; Wang et al., 2018; Yin et al., 2019; Zhang et al., 2018).

Ion channels carry electric current across the cell membrane in the form of diffusing ions; both selective filter and channel gate are the key structural elements of ion channels (Zheng and Trudeau, 2015). Upon ligand binding and channel opening, how ions permeate through the TRPM2 channel remains elusive. Although several studies have revealed the structure of the selectivity filter of both nvTRPM2 and drTRPM2 (Figures S3D and S3E), it is not delineated in the hsTRPM2 structure, which is likely due to higher flexibility of this domain (Huang et al., 2018; Wang et al., 2018; Yin et al., 2019; Zhang et al., 2018). Moreover, nvTRPM2 is highly selective for calcium ions with a PCa^{2+}/PNa$^+$ of ∼35, but the calcium selectivity in hsTRPM2 (PCa^{2+}/PNa$^+$ ∼0.45) is much lower (Zhang et al., 2018). Therefore, the conformation of selectivity filter in hsTRPM2 may be distinct from that of nvTRPM2. Furthermore, in its close homolog TRPM8 channel, the conformation of

the selectivity filter was also largely obscure, which was resolved only in the calcium-bounded desensitized state (Diver et al., 2019). Both TRPM2 and TRPM8 channels are permeable to divalent cations like calcium (McKemy et al., 2002; Nagamine et al., 1998), whereas the TRPM4 channel conducts only monovalent cations, such as sodium and potassium (Launay et al., 2002). Although the selectivity filter of TRPM4 has been clearly resolved (Guo et al., 2017), the lack of structural information in the selectivity filter of hsTRPM2 impedes our understanding of the mechanisms underlying ion selectivity in TRPM channels in mammals. Therefore, revealing the architecture of pore domain in hsTRPM2 would largely advance our knowledge of this important ion channel.

Here we report the cryo-EM structure of the full-length hsTRPM2 channel in lipid nanodisc in ligand-free state. Using the structure-guided computational modeling and electrophysiology assays, we identified a quadruple-residue motif (^{979}FGQI^{982}) as the ion selectivity filter. We further performed substituted cysteine accessibility assays to show that the selectivity filter also works as an upper gate in hsTRPM2, but not in nvTRPM2. Our study provides new insights into the gating mechanism in the TRPM2 channel and highlights a striking structural difference in the gating process of mammalian and non-mammalian TRPM2 channels.

RESULTS

Structure of the *hs*TRPM2 channel in nanodisc

To capture the hsTRPM2 structure in lipid environments, we first reconstituted hsTRPM2 into lipid nanodisc and then determined its cryo-EM structure in the presence of EDTA (see STAR Methods; Figure S1). The 3.76-Å resolution map of hsTRPM2 in the ligand-free state is of high quality in the bulky cytosolic N-terminal domain (NTD) and C-terminal domain (CTD) and major parts of the transmembrane domain (TMD) (Figures 1B and S1). The overall architecture of the homo-tetrameric hsTRPM2 channel complex has three dimensions of approximately 118 × 118 × 151 Å, composed of three layers (Figures 1B–1E, S2A, and S2B). The S1-S6 TMD and the adjacent TRP domain constitute the top layer (Figures 1B–1G). The TMD positions a canonical domain-swapping conformation, with the peripheral S1-S4 domain in one subunit sitting next to the central S5-S6 domain from the neighboring subunit (Figures 1B and 1C). Before the TMD, the NTD consists of four TRPM homology region (MHR) repeats (Figures 1A–1E). With a central β sheet surrounded by several α helices, the major part of MHR1/2 adopts the Rossmann-like fold. MHR3/4 is composed of 16 α helices

Figure 1. The overall architecture of *hs*TRPM2 in nanodisc
(A) Domain organization of hsTRPM2 channel with residue numbers. The dashed square indicates the less determined region.
(B) The cryo-EM map of the full-length hsTRPM2 channel. Each subunit is shown in different colors.
(C) The cartoon model of hsTRPM2 channel in nanodisc in side (left), top (upper right), and bottom (bottom right) views.
(D) Topology diagram delineating the protein domains with secondary structure elements. The dashed line shows that the selectivity filter and outer pore loop are not built in the model.
(E) The structure of one hsTRPM2 subunit.
(F) The superimposition of density map and model in TMD (side view); the dashed area indicates the TMD of monomer hsTRPM2.
(G) The superimposition of density map and model in pore region (left: top view; right: side view). The red dashed circle indicates the indirectly modeled selectivity filter and outer pore loop (SF-loop) with several scattered densities between pore helix and S6.
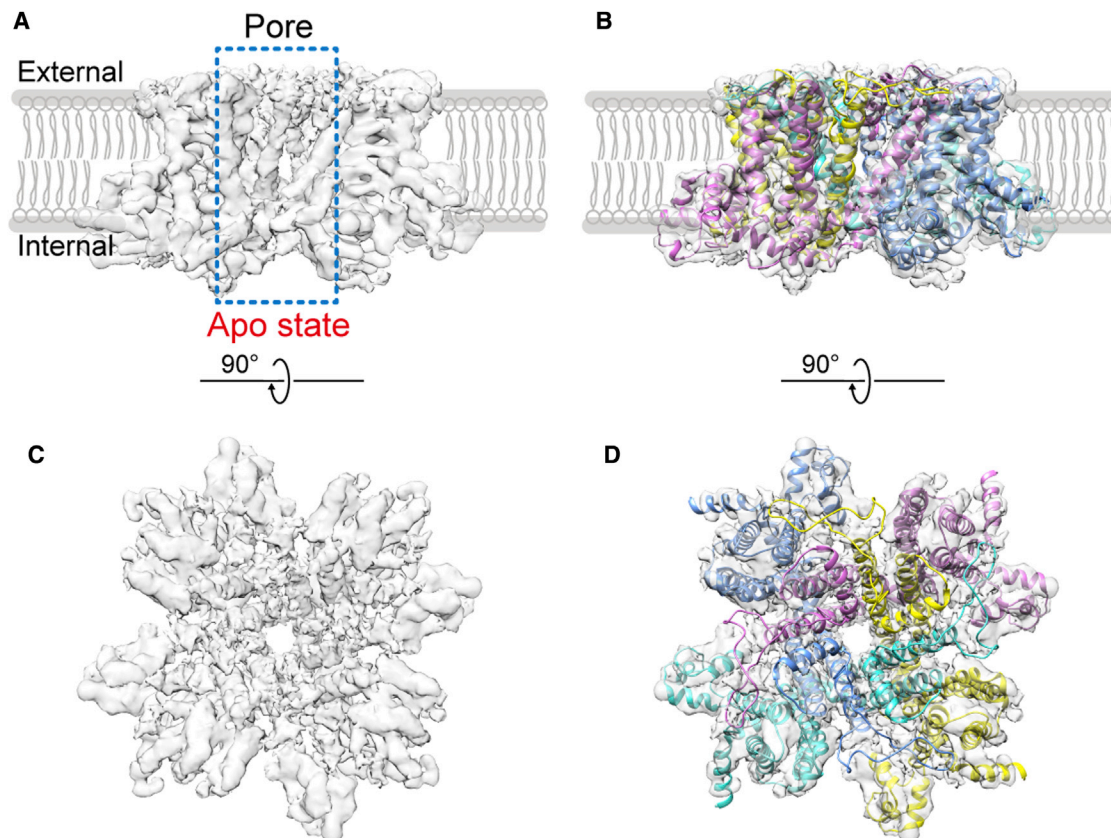
Figure 2. The EM density-guided modeling of pore region using Rosetta

(A and C) The EM density maps of TMDs of ligand-free *hs*TRPM2 channel structure in nanodisc (A: light gray, side view; C: light gray, top view).

(B and D) The overlay of EM density maps and structure models of TMD in the ligand-free state in different perspectives (B: side view; D: top view). The structure models of selectivity filter loop in pore region are calculated and reconstructed by Rosetta based on EM density maps in (A) and (C).

and is sandwiched by the TMD and two MHR1/2 domains from its own and the adjacent subunits. Following the TMD, the CTD contains a long rib helix, a coiled-coil helix, and a NUDT9-H domain (Figures 1C–1E). The NUDT9-H and MHR1/2 domains constitute the bottom layer, whereas the MHR3/4 domains form the middle layer. All the MHR1/2, MHR3/4, and NUDT9-H domains participate in tetrameric assembly and make up a large cytosolic square ring, with the four coiled-coil helices running through the central hole (Figures 1B–1E).

In the TMD, most transmembrane helices, including the S1-S4 domain, S4-S5 linker, S5, and major parts of S6, are well resolved (Figures 1B, 1F, and 1G). Densities in the pore helix and S6 N-terminal end are of low quality, and poly-alanines are modeled in these regions. The filter and outer pore loop are still invisible in the current map, similar as those observed in *hs*TRPM2 structures determined in detergent micelle (Figure 1G) (Huang et al., 2019; Wang et al., 2018). In comparison with the ligand-free *hs*TRPM2 structure determined in detergent (PDB: 6PUO and 6MIX), our *hs*TRPM2 channel structure in nanodisc adopts the same conformation in the NTD and CTD, whereas its S1-S4 domain is 2–4 Å closer to the pore domain, forming a more condensed TMD (Figures S2A–S2F). The conformational difference in the TMD between two ligand-free *hs*TRPM2 chan-

nels may arise from different sample preparation conditions. As the lipid nanodisc mimics the *in vivo* membrane environment, our *hs*TRPM2 structure may represent a more physiological ligand-free state.

Delineation of the pore structure by cryo-EM-guided modeling

The ion-conducting pore of an ion channel is a key structural unit for its function and physiological roles, in which the selectivity filter determines ion selectivity and/or permeation (Yang and Cui, 2015). In our structures, like all *hs*TRPM2 channel structures recently reported (Figures 1 and S1) (Huang et al., 2019; Wang et al., 2018), the selectivity filter was not directly observed, probably because of high structural flexibility. In order to better delineate the selectivity filter structure, we took an integrative approach, starting with first generating a soft mask covering the TMD and subtracting the density outside these regions from the raw particles in Relion. Later, 3D refinement was performed by aligning these "subtracted particles" based on the remaining density to boost local resolution of TMD to 3.68Å, which allowed us to clearly view the pore domain arranged in the closed conformation (Figures 2A, 2C, and S1). Based on such an

improved map of TMD, we performed computational modeling of the selectivity filter.

We performed *de novo* modeling of the pore loop between the end of the pore helix and the beginning of S6, consisting of residues 978–1,024, with cyclic coordinate descent (CCD) and kinematic loop relax protocol (KIC) loop modeling using the Rosetta Suite (Leaver-Fay et al., 2011) (see STAR Methods). The fitness of the residues in the structural models with the 3D map was evaluated as a scoring term in Rosetta (DiMaio et al., 2015; Wang et al., 2015). The models of the pore structure with the lowest energy match well with the 3D maps (Figures 2B and 2D). Examination of the resulting pore structural models in a ligand-free state enables us to identify a quadruple-residue motif, composed of F979, G980, Q981, and I982, to form the selectivity filter (Figures S2G–S2I). This motif is also highly conserved in TRPM4 and TRPM8 and constitutes the selective filter of *hs*TRPM4 (FGQI) and *pm*TRPM8 (FGQY), respectively (Figures S3A–S3C) (Autzen et al., 2018; Diver et al., 2019).

Furthermore, plotting of the radius along the transmembrane pore reveals two restrictions that may control ion movement, which we refer to as the upper and lower activation gates (Figures S2H and S2I). The FGQI motif serves as the upper gate and the selectivity filter. The pore radius at the selectivity filter is 0.56 Å in the ligand-free state (Figure S2I). The restriction at the S6 bundle crossing acts as the lower gate similar to previously reported TRPM2 structures (Figure S2I) (Huang et al., 2019; Wang et al., 2018). To provide evidence to support the predicted dual role of the FGQI motif as the selectivity filter determining ion selectivity and as an activation gate controlling ion flow in the *hs*TRPM2 channel, we examined the pore function using patch-clamp recording in combination with site-directed mutagenesis.

Functional validation of the FGQI motif as the selectivity filter

We first performed alanine screening assay for the pore turret and pore helix region (F967-E994) of *hs*TRPM2, which showed the G980A, Q981A, and I982A mutants were still functional, while the F979A mutant was non-functional (Figure S4A). Our study thus mainly focused on evaluating the GQI motif as the selectivity filter by measuring the reversal potential (E_{rev}) of ADPR-induced whole-cell currents in HEK293 cells expressing wild-type (WT) or mutant *hs*TRPM2 channels in extracellular Ca^{2+} solutions or Na^+ solutions, which reflects the ion selectivity to Ca^{2+} over Na^+ of the open channel, PCa^{2+}/PNa^+ (Figures 3 and S4B–S4E). Indeed, mutation of G980 or Q981 to various residues significantly decreased or increased the reversal potential, respectively (Figure 3). Specifically, relative permeability of G980 mutants (G980A/C/S) to Ca^{2+} decreased because of the increase of side chain, which affected more on Ca^{2+} than Na^+ (Figure 3B). Q981 mutations (Q981A/E/N) increased the permeability of Ca^{2+}, which might be caused by reducing the side chain or introducing the carboxy group, because Ca^{2+} carries two positive charges and is more sensitive to the acidic or nucleophilic group (Figure 3B). To further exclude any contamination from the endogenous background currents or membrane leak, we recorded the current induced by intracellular solution without ADPR or with extracellular *N*-(p-amylcinnamoyl) anthranilic acid (ACA) perfu-

sion, both of which showed a negligible current (Figures S4F and S4G).

For residue I982 localized at the extracellular entrance of the selectivity filter, replacement by residues with reduced side-chain size (I982A and I982S) or introducing negative charge (I982E) altered the reversal potential (Figure 3). By contrast, substitution by residues with similar side-chain properties (I982L and I982F) had no effect, which was consistent with the alteration of PCa^{2+}/PNa^+ for those mutants and also indicated that the side chain may be involved in the structural stability of selective filter in open state (Figure 3). As controls, mutation of G984, Y985, or I986 residues next to but outside the selectivity filter or even introduction of previously reported triple-residue substitutions ([984]GY[985] of *hs*TRPM2 substituted by the corresponding residues L, D, and E from *nv*TRPM2) (Tóth and Csanády, 2012) resulted in no change in the reversal potential and PCa^{2+}/PNa^+ (Figure 3). Taken together, these results are in strong support of the importance of the FGQI motif in determining the ion selectivity of the *hs*TRPM2 channel, as predicted by our structural model of the pore domain (Figures S2G–S2I).

To further validate the [979]FGQI[982] as the selectivity filter, we also measured single-channel conductance on the assumption that if a residue in the selectivity filter is critical for ion selectivity, its mutation may alter single-channel conductance (Zheng and Sigworth, 1997). In agreement with measurement of the ion selectivity, the G980A/S and Q981A/E mutations gave rise to significant effects on single-channel conductance (Figures 4 and S5). Among them, G980A mutation reduced the single-channel conductance of Na^+ and Ca^{2+}, which might be a result of the introduction of the non-polar side chain hindering the passage of cations (Figure 4). Q981A mutation changed only the single-channel conductance of Ca^{2+}, which was likely due to the lack of the side chain that was critical for Ca^{2+} passing through the selective filter (Figure 4). Intriguingly, G980S and Q981E exhibited a smaller conductance in the physiological extracellular Na^+-containing solution but was not noticeably affected in the presence of a high extracellular Ca^{2+} concentration, which might reflect the differential electrostatic interactions of introduced hydroxyl or carboxy group with the permeant cations (Figures 4 and S5). Mutations on residue I982 resulted in negligible changes in single-channel conductance (Figure 4). This is likely due to the location of this residue at the entrance of the selectivity filter, which is away from the core of the selectivity filter critical for ion permeation. Similarly, the residue Y985 is localized farther away outside our predicted selectivity filter (Figure S2G), and its mutant Y985A exhibited the approximate single-channel conductance as WT channel (Figures 4 and S5). Collectively, these results from analysis of the effects of mutating G980, Q981, and I982 on the ion selectivity and single-channel conductance support that this FGQI motif acts as the selectivity filter in the *hs*TRPM2 channel.

The selectivity filter serves as the upper gate

Delineation of the pore structures using cryo-EM map-guided computational modeling further predicts that the selectivity filter is narrow in the closed state and likely forms as a gate (Figures S2H and S2I). As suggested by a recent study of the TRPV1-3

A

B
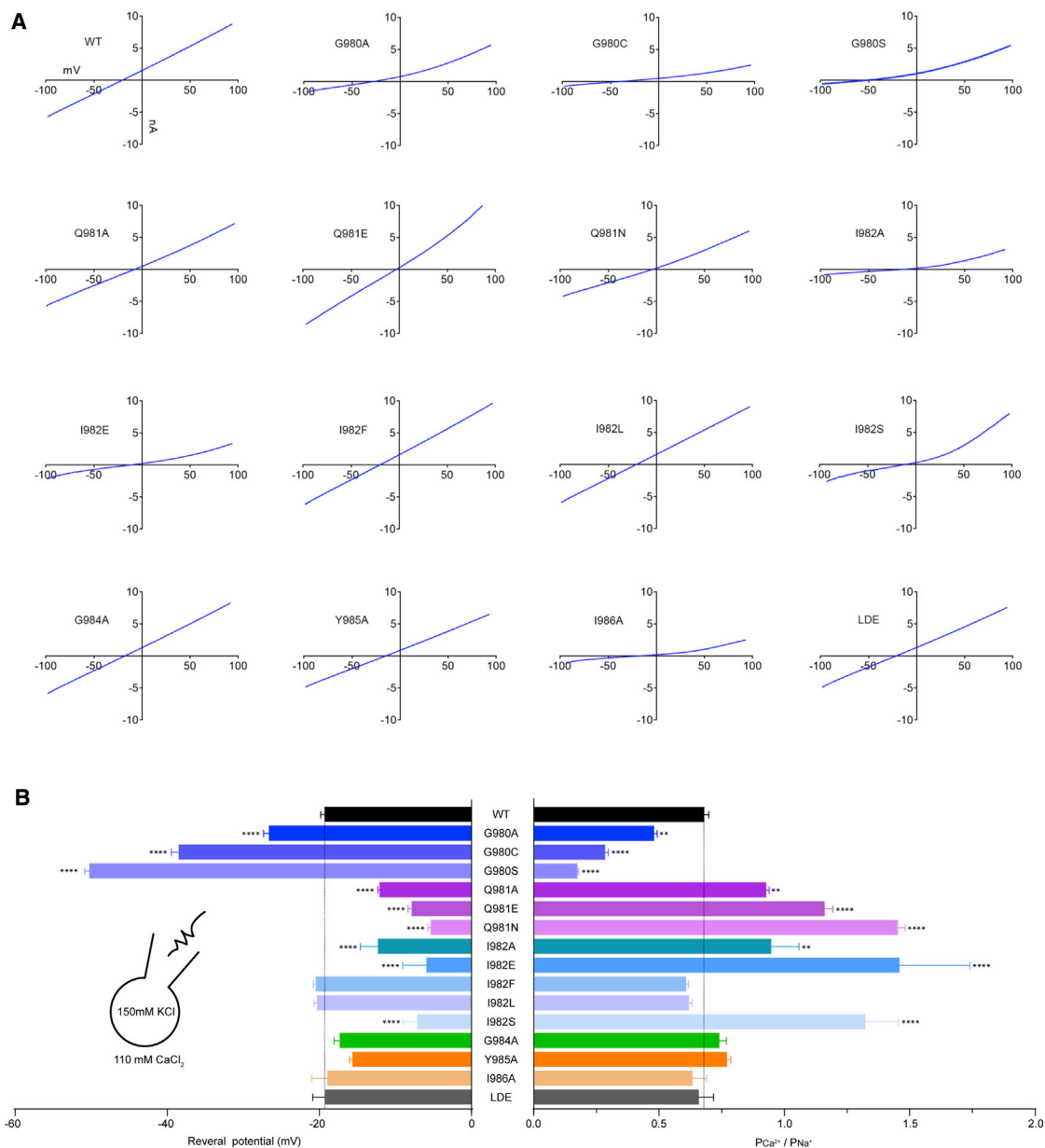
Figure 3. The selectivity filter of the *hs*TRPM2 channel locates at F979-I982

(A) I-V (current-voltage) relationships of WT and mutant channels induced by W-K-ICS with 500 μM ADPR from −100 mV to 100 mV in extracellular 110 mM CaCl$_2$ (blue lines).

(B) Summary of reversal potential (RP, left) and the PCa^{2+}/PNa$^+$ (right), derived from Equations S2–S6. The dotted lines show the mean values of the WT channel. The inset diagram indicates whole-cell recording patch-clamp mode and the intra- and extra-cellular solution. The number of cells examined in each case are over three (n ≥ 3). **p < 0.01, ***p < 0.001, ****p < 0.0001, when compared with WT group. Data are presented as mean ± SEM.

channels, extracellular ions may still pass the pore at the selectivity filter with a relatively small radius (Jara-Oseguera et al., 2019). To test whether the selectivity filter genuinely acts as a gate limiting ion flow in the *hs*TRPM2 channel, we used the substituted cysteine accessibility method (SCAM) in conjunction with Ag$^+$, a cysteine-modifying ion with an atomic radius value (1.26 Å) that is similar to but slightly larger than that of Na$^+$ (0.97 Å) (Salazar et al., 2009). Such an approach has been

applied to pinpoint the activation gate in numerous channels, including TRPV1 (Jara-Oseguera et al., 2019; Liu et al., 1997; Salazar et al., 2009).

We introduced cysteine substitution at residues in the S6 positioned below the selectivity filter. Although many mutant channels were either non-functional or the ADPR-induced currents were rapidly inactivated (Figures S6A, S6G, and S6J), three mutant channels (F1035C, I1038C, and I1045C) mediated robust
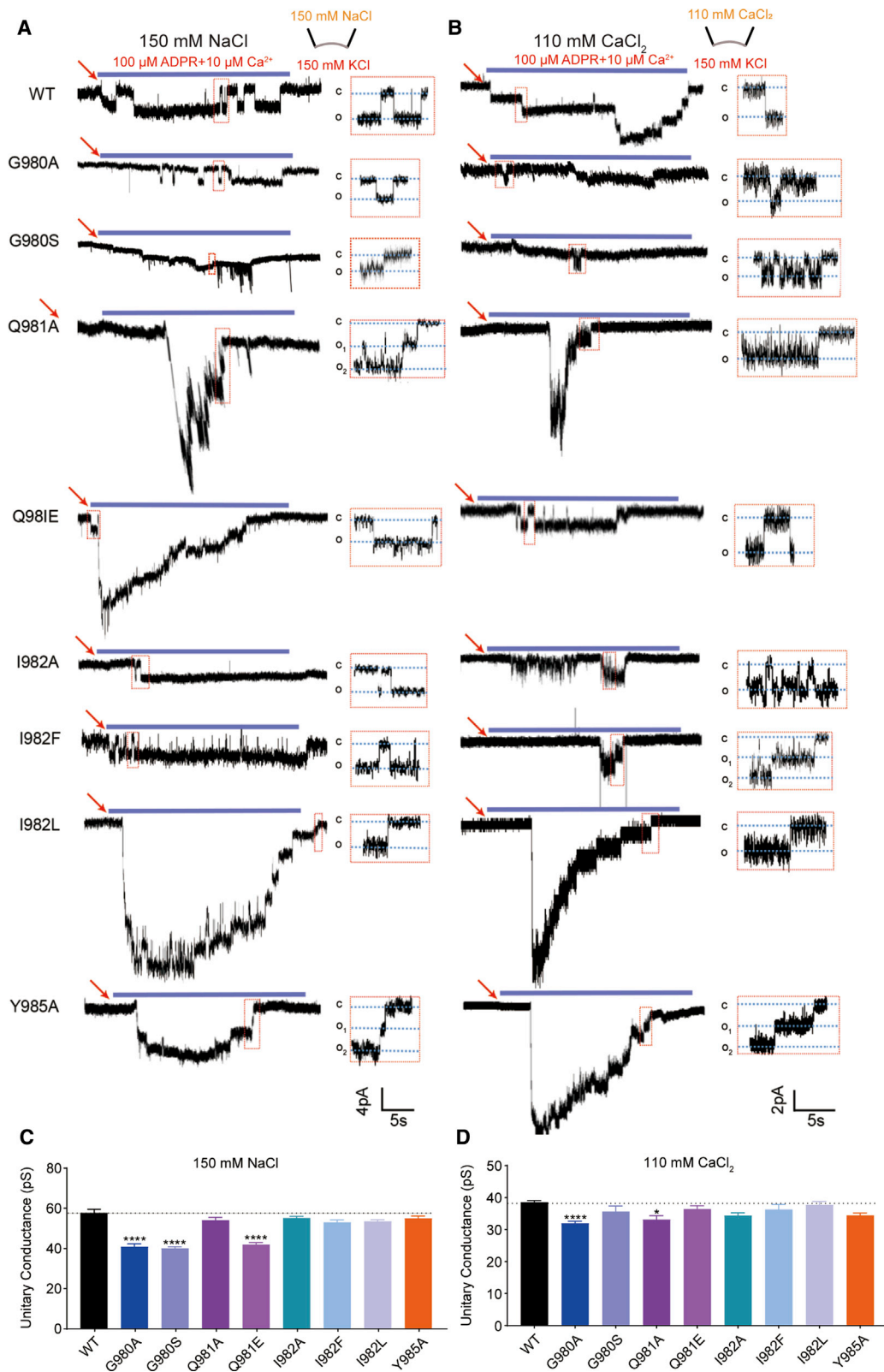
(legend on next page)

ADPR-induced currents with modest inactivation (Figures 5C, S6A, S6D, S6E, and S6I). Exposure of the WT channel to extracellular Ag$^+$ before (bath or pre-incubation) and during channel opening (open) caused a negligible effect on ADPR-induced current amplitude or the rate of current inactivation (Figures 5B, 5D, 5K, and S6L). Similarly, exposure to Ag$^+$ using three different protocols had no effect on ADPR-induced currents for the I1038C mutant channel (Figures 5G, 5H, 5K, and S6M). Such results indicate that Ag$^+$ modification did not occur on the endogenous cysteines in the WT channel or on the introduced cysteine in the I1038C mutant channel, or alternatively, such Ag$^+$ modification did not perturb channel activation.

Exposure of the F1035C and I1045C mutant channels to Ag$^+$ in the open state, introduced by using open or pre-incubation protocols, led to similar effects on ADPR-induced currents, which, however, decreased at a faster rate as compared with ADPR-induced currents when Ag$^+$ was applied only before the channel activation (Figures 5E, 5F, 5I–5L, S6N, and S6O). Such Ag$^+$-induced accelerated current inactivation cannot be reversed by washing, consistent with covalent modification by Ag$^+$ of introduced cysteines (Figure S6K), where Ag$^+$ forms nearly irreversible complexes with cysteine residues and could elicit additional conformational rearrangements to cause change of inactivation rate. The residue I1045 is close to the intracellular gate and points toward the center of the pore, and so it is readily accessible to modification by Ag$^+$ (Figure 5C). Although the residue F1035 faces to the opposite sides of the S6 helix, it is accessible to Ag$^+$ in the central cavity likely through the fenestration, as shown in Figure S6B. These results show that F1035C and I1045C deep in the pore were inaccessible to extracellular Ag$^+$ when the channel was in the closed state and became available to Ag$^+$ after the channel opened (Figure 5C), supporting the notion that the selectivity filter forms a bona fide gate in the hsTRPM2 channel that restricts ion flow in the closed state and widens in the ADPR/Ca^{2+}-bound open state. This finding is in contrast with the cryo-EM structure of the nvTRPM2 channel, where the selectivity filter adopts a conformation with a pore radius large enough for ion permeation even in the closed state (Figure S3D) (Zhang et al., 2018).

To validate such a species-dependent structural or conformational difference, which is important to our understanding of the TRPM2 channel gating, we also applied SCAM to probe the nvTRPM2 channel pore. Cysteine substitution was introduced in several residues on the S6 below the selectivity filter (V1071, F1072, I1075C, L1078, L1081, and I1082) (Figure 6B). All mutant channels were functional (Figures 6C–6E, S7A–S7D, and S7G). Exposure to Ag$^+$ in either the closed or open states resulted in no changes in ADPR-induced activation and inactivation kinetics, except the F1072C and I1082C mutant channels (Figure S7F). For the F1072C mutant channel, exposure to Ag$^+$ starting in the closed state profoundly delayed ADPR-induced channel activation (Figures 6D, 6F, 6G, S7E, and S7F), clearly

suggesting that extracellularly applied Ag$^+$ can enter deep into the central cavity even in the closed state. Exposure to Ag$^+$ in the open state slowed down the inactivation of the I1082C mutant (Figures 6G, S7D, and S7F). These results are consistent with the cryo-EM structures of the nvTRPM2 channel, where the selectivity filter is ion-permissive in the closed state (Zhang et al., 2018). Overall, our structural and functional evidence support that the selectivity filter in the hsTRPM2 channel adopts a more restrictive conformation in the closed state and serves as a gate for ion permeation (Figures 5 and 7), which is distinct from nvTRPM2.

DISCUSSION

In this study we present the first structure of the full-length hsTRPM2 channel embedded in nanodisc in the ligand-free state. Such a 3.7-Å resolution map is of high quality in the bulky cytosolic NTD and CTD and major parts of the TMD, except the filter and outer pore loop (Figures 1B, 1F, 1G, and S1). Both in detergent or nanodisc, the invisibility of the filter and outer pore loop may reflect the intrinsic flexibility, which cannot be legibly captured under cryo-EM. Small molecules, auxiliary subunits, or pore-region-targeted antibody may help stabilize this region and facilitate structure determination.

The functions of ion channels depend on their capacity to permeate ions across cell membranes in response to specific signals; however, it is important to uncover the selective filter property of the hsTRPM2 channel for understanding its gating mechanism (Yang and Cui, 2015). To determine the selective filter of hsTRPM2, we first yielded an EM map of the TMD of the hsTRPM2 channel with a resolution of 3.68 Å (Figures 2A and 2C). Then, a cryo-EM map-guided computational modeling approach has enabled us to extract structural information of the TMD, particularly the ion-conducting pore (Figures 2B and 2D). We can readily identify that the conformation of the pore is in the ligand-free, closed state (Figures S2G–S2I). Structural modeling of the pore led to identification of the FGQI motif as the selectivity filter (Figures S2G–S2I). Electrophysiological characterizations using patch-clamp recording show that mutation of this motif significantly altered the ion selectivity, reflected by the change in the reversal potential of ADPR-induced whole-cell currents (Figures 3 and S4), ion conductance measured by single-channel recordings (Figures 4 and S5), or both. Particularly, the Q981E mutation enhanced the permeability of Ca^{2+} over Na$^+$, supporting that introduction of negative charge facilitates Ca^{2+} selectivity in the open hsTRPM2 channel as proposed in our previous study (Xia et al., 2008). Overall, our electrophysiological characterizations provide functional evidence to support the FGQI motif as the selectivity filter determining the ion selectivity.

Ion channels activated by their respective stimuli open an S6 helix gate at the cytosolic side of the pore; however, a selectivity filter at the extracellular side of the pore also forms the channel

---

Figure 4. Permeation and single-channel properties of the hsTRPM2 channel

(A and B) Representative single-channel recordings in WT or mutant channel-expressing HEK293T cells exposed to 100 μM ADPR and 10 μM Ca^{2+} in extracellular 150 mM NaCl (A) or 110 mM CaCl$_2$ (B). The red arrows in each panel indicate the time point at which ADPR and Ca^{2+} were perfused.

(C and D) Summary of unitary conductance, derived from single-channel recording shown in (A) and (B) via Equation S1. The number of cells examined for each case are over three (n ≥ 3). **p < 0.01, ***p < 0.001, ****p < 0.0001, when compared with WT group. Data are presented as mean ± SEM.
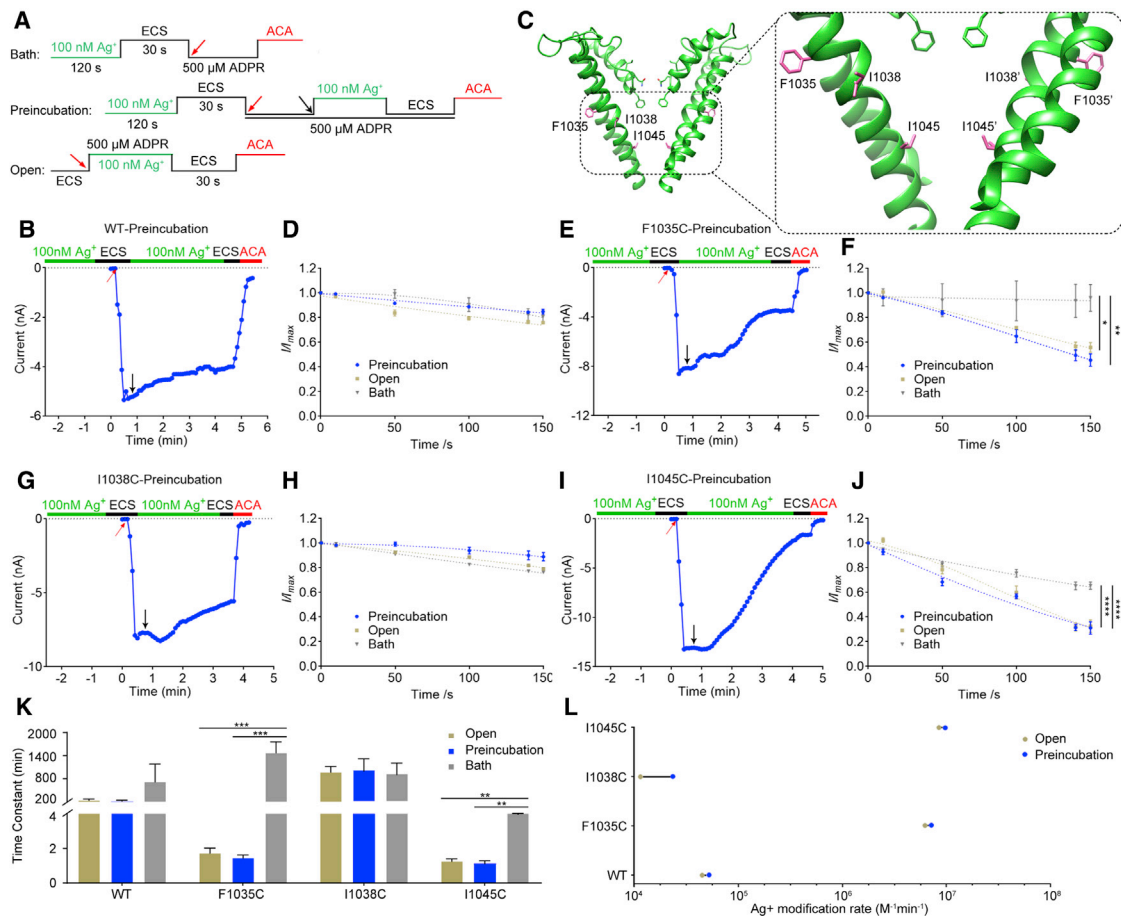
Figure 5. The selectivity filter is an activation gate in the *hs*TRPM2 channel

(A) Experimental protocols for whole-cell patch-clamp recording with Ag⁺ modification in the open and pre-incubation (closed) states (lower) or not (bath). When the ADPR-evoked currents reach the steady-state, 100 nM Ag⁺ was perfused for modification in open states. The red arrows in each panel indicate the time point at which whole-cell configuration was established. The black arrow represents that the Ag⁺ treatment was given.

(B, E, G, and I) Representative ADPR-evoked currents at -80 mV (denoted by blue circles) in pre-incubation state, obtained by voltage ramps every 5 s, from cells expressing WT, F1035C, I1038C, or I1045C mutant channel in extracellular solution containing 150 mM NaNO₃. The horizontal bars here and in the other panels indicate perfusion of Ag⁺ (100 nM; green bars), ECS (bath solution, ECS: 150 mM NaNO₃; black bars), and ACA (20 μM; red bars).

(C) Cartoon representation of side-chain orientation of F1035, I1038, and I1045 residues (shown as sticks) in ligand-free state.

(D, F, H, and J) Time courses of the normalized current of WT, F1035C, I1038C, and I1045C mutants with application of 100 nM Ag⁺ (blue, khaki filled circles) or not (gray filled circles) from experiments as in (B), (E), (G), (I), and Figures S6L–S6O, respectively. Dotted lines (blue and khaki) represent single-exponential fits to the cumulative modification of pre-incubation and open states. The bath (gray dashed line) reflects current rundown caused by spontaneous de-activation of channels.

(K) Summary of time constant of current de-activation with Ag⁺ modification at -80 mV in pre-incubation (blue) and open (khaki) states or bath (gray) from experiments in (B), (D)–(F), and Figures S6L–S6O.

(L) Comparison of Ag⁺ modification rates in the open state without (khaki symbols) or with pre-incubation of silver ions in the closed state (blue symbols) obtained from (B), (E), (G), (I), and Figures S6L–S6O. The number of cells examined for each case is three or more (n ≥ 3).

*p < 0.05, **p < 0.01, ***p < 0.001, ****p < 0.0001. Group data are presented as mean ± SEM. ACA, N-(p-amylcinnamoyl) anthranilic acid (non-specific inhibitor of the TRPM2 channel); ECS, extracellular solution; I, current obtained after treatment with Ag⁺; I_{max}, steady-state current obtained at t = 0 with 500 μM ADPR and 100 nM Ag⁺; ns, no significant difference when compared with WT. See also Figure S6.

gate in some channels (Abderemane-Ali et al., 2019; Bernèche and Roux, 2005; Dutzler et al., 2003; Kopec et al., 2019; Pippel et al., 2017; Tao et al., 2017). Our results using SCAM showed that extracellular Ag⁺, with an atomic radius slightly larger than Na⁺, can reach cysteines (F1035C and I1045C) introduced beneath the selectivity filter only in the open state, but not in the closed state, of the *hs*TRPM2 channel (Figures 5E, 5F, 5I–5L, S6N, and S6O). Therefore, the selectivity filter sufficiently

narrows to restrict ion flow and expands accompanying channel activation. Such an ion-restrictive conformation at the selectivity filter of the *hs*TRPM2 channel pore in the closed state differs noticeably from the widened conformation of the selectivity filter in the *nv*TRPM2 structure in the closed state (Figures 6B and S3D) (Zhang et al., 2018). This is consistent with our SCAM results that extracellular Ag⁺ readily enters to modify the cysteines (F1072C and I1082C) introduced deep in the central cavity of the
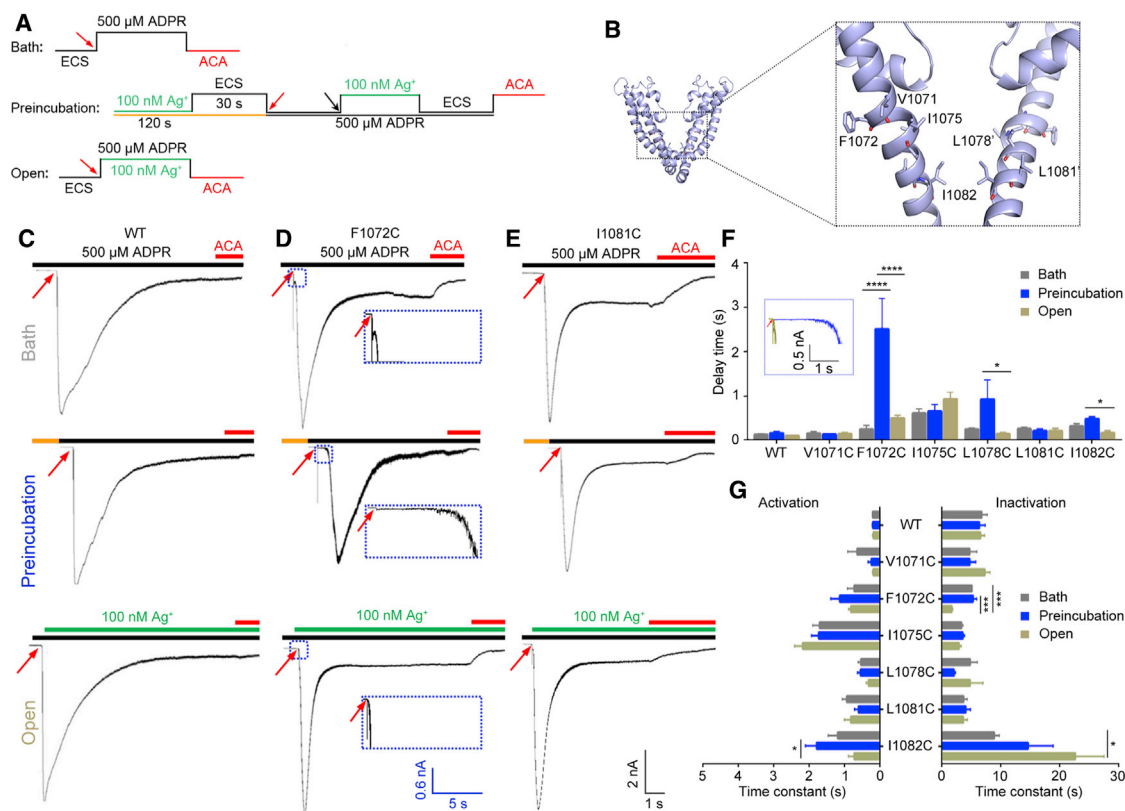
Figure 6. The selectivity filter is a pseudo-gate in the *nv*TRPM2 channel

(A) Experimental protocols for whole-cell patch recording with Ag⁺ modification in the open and pre-incubation states (middle and lower) or not (upper). Ag⁺ was pre-incubated for 120 s and washed by ECS for 30 s before whole-cell patch recording in the pre-incubation state in the presence of 500 μM ADPR with the membrane potential held at −60 mV. 100 nM Ag⁺ was applied for modification in the open state at the same time the whole-cell configuration was established.

(B) Cartoon representation of side-chain orientation of V1071, F1072, F1075, I1078, L1081, and I1082 residues (shown as sticks) in Ca²⁺-bound state (light blue, PDB: 6CO7).

(C–E) Representative ADPR-evoked currents at −60 mV (black lines) in bath, pre-incubation, and open states from cells expressing the WT, F1072C, and L1081C mutant channels in extracellular solution containing 150 mM NaNO₃. The red arrows in each panel indicate the time point at which whole-cell configuration was established. The short orange bar represents the process of Ag⁺ modification and ECS wash of pre-incubation state indicated in (A) (middle orange bar).

(F) Summary of the delay times in bath, pre-incubation, and open states in (C)–(E) and Figures S7A–S7D. The inset represents the overlay of initial activation course of channel in pre-incubation state for WT, F1072C, and L1081C channels (blue dotted box in C–E).

(G) Summary of the activation time constants (τ_a, left) and inactivation time constants (τ_i, right) in bath, pre-incubation, and open states in (C)–(E) and Figures S7A–S7D.

The number of cells examined in each case is three or more (n ≥ 3). *p < 0.05, **p < 0.01, ***p < 0.001, ****p < 0.0001. Data are presented as mean ± SEM. ns, no significant difference when compared with each other. See also Figure S7.

*nv*TRPM2 channel in the closed state, indicating that the pore at the selectivity filter is highly ion permissive, so it is not a gate (Figures 6D, 6F, 6G, and S7D–S7F). We revealed a clear and functionally important difference in the selectivity filter between the *hs*TRPM2 and *nv*TRPM2 channels (Figures 5, 6, and 7). A previous study has reported that the cation permeability of the *nv*TRPM2 is higher than that of the *hs*TRPM2, being coincident with the larger pore diameter and the larger negative surface charge density in the vestibule of the *nv*TRPM2 channel (Zhang et al., 2018). The relatively poor selectivity of cations in TRPM2 might indicate that under the physiological condition, instead of selecting different cations, its selectivity filter serves as a gate to control ion permeation (Figure 3B). These functional results collectively suggest that the pore conformation substan-

tially differs in *hs*TRPM2 and *nv*TRPM2 channels. The dual function of the selectivity filter of *hs*TRPM2 is also different from that of the *Rattus norvegicus* TRPV1 (*rn*TRPV1) filter (Figures S3F and S3G), which undergoes conformational change during the channel opening (Jara-Oseguera et al., 2019; Salazar et al., 2009) but is permeable to ions in the closed state as suggested by a recent study (Jara-Oseguera et al., 2019). Such a functional difference most likely arises from the less homologous in sequence and conformation (Figures S3F and S3G).

In conclusion, our study has resolved the *hs*TRPM2 structure in nanodisc in the ligand-free state and computationally modeled the structure of the selectivity filter. We further provide functional evidence to support the selectivity filter as a gate in the *hs*TRPM2 channel, species difference in the pore structure, and gating in
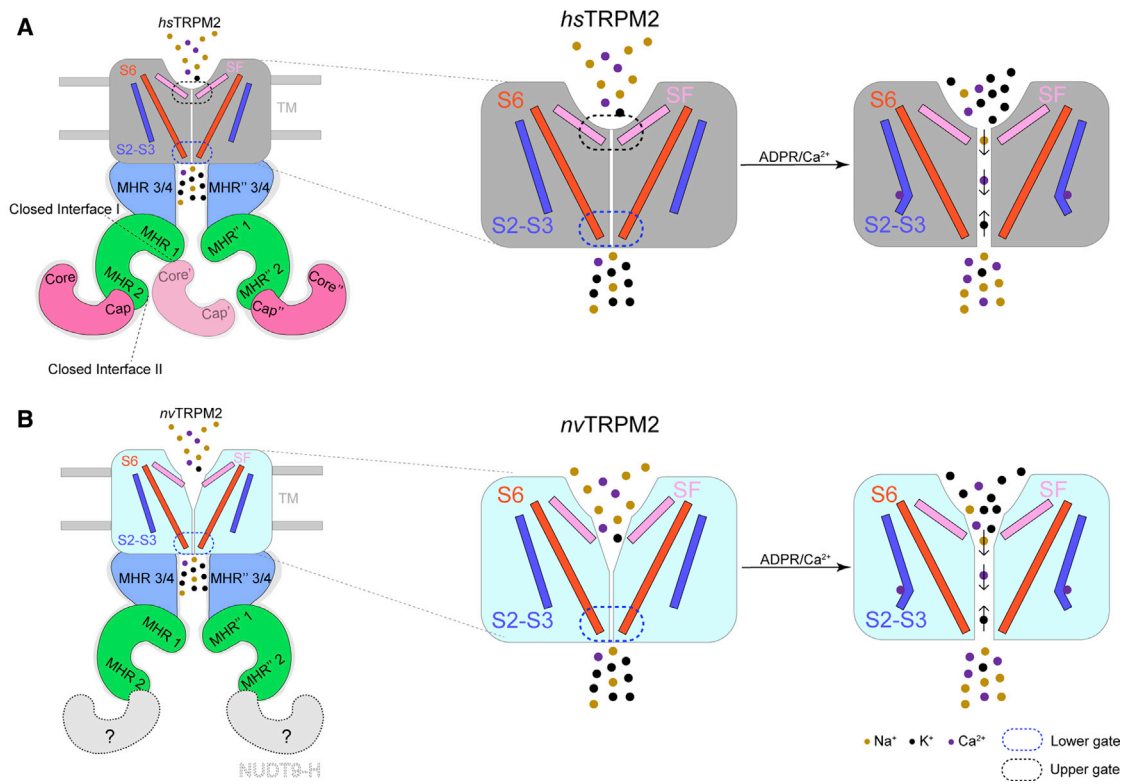
Figure 7. The gating mechanism of *hs*TRPM2 by ADPR and calcium
(A and B) Cartoon representation of pore region conformational changes in *hs*TRPM2 and *nv*TRPM2 channels induced by ADPR and Ca²⁺, respectively. Left panel, the side view of overall cartoon structures with colored domains. Middle and right panels, zoomed-in views of pore region conformational changes induced by ADPR and calcium. The dashed gray circle with a question mark in (B) indicates the unresolved NUDT9-H domain in the *nv*TRPM2 structure.

the TRPM2 channels. Our study has demonstrated the feasibility of combining cryo-EM, computational modeling, and functional assays to extract structural information of functionally important but highly dynamic domains and thereby provides mechanistic understanding of the function of ion channels and potentially other membrane proteins.

Limitations of the study

Although we have largely improved the overall quality of our TRPM2 cryo-EM density map with the lipid nanodisc, the quality of map in specific regions, such as the selectivity filter and the outer pore loop, still limits our in-depth interpretation of the structure. We reasoned that mostly likely it reflects the intrinsic flexibility in these regions. We expect that small molecules or peptides targeting the outer pore region of TRPM2 will be developed in the future, which would help stabilize the outer pore of TRPM2. Moreover, although we built up the models of the pore structure by performing *de novo* modeling of the pore loop with CCD and KIC loop modeling using the Rosetta Suite, it is not the real structure of TRPM2. In addition, as we have determined TRPM2 structure only in the apo state, our interpretation of the gating mechanism and function in TRPM2 could be further strengthened by resolving the channel in other physiologically or pathologically relevant states, such as the ligand-bound open state.

STAR★METHODS

Detailed methods are provided in the online version of this paper and include the following:

- KEY RESOURCES TABLE
- RESOURCE AVAILABILITY
  - Lead contact
  - Materials availability
  - Data and code availability
- EXPERIMENTAL MODEL AND SUBJECT DETAILS
  - Cell lines
  - Human TRPM2 construct design
- METHOD DETAILS
  - Cell culture
  - Expression and purification
  - Electron microscopy sample preparation and data acquisition
  - Electron microscopy data processing
  - Computational modeling
  - Electrophysiology
  - Ag⁺-modification assay
  - hsTRPM2 Ag⁺ modification procedures
  - nvTRPM2 Ag⁺-modification procedures
- QUANTIFICATION AND STATISTICAL ANALYSIS

AUTHOR CONTRIBUTIONS

W.Y., J.G., and F.Y. designed the research; X.Y. conducted and contributed most of the experiments, including *hs*TRPM2 expression, purification, cryo-EM data collection, functional assays (patch-clamp recording and Ag$^+$ modification), and data analysis; X.Y., C.M., L.L., L.X., Y.L., L.Z., and X.G. contributed to *hs*TRPM2 expression, purification, and lipid nanodisc reconstitution; X.Y., Y.X., X.Z., and J.G. contributed to cryo-EM data collection and structural analysis; F.Y. and W.Z. performed the pore region reconstruction; X.Y. and J.Z. performed the patch-clamp recording; W.Y., L.-H.J., F.Y., J.G., and Y.N. participated in discussion and interpretation of the data and revised the manuscript; W.Y., X.Y., F.Y., and J.G. prepared the paper.

REFERENCES

Abderemane-Ali, F., Findeisen, F., Rossen, N.D., and Minor, D.L., Jr. (2019). A Selectivity Filter Gate Controls Voltage-Gated Calcium Channel Calcium-Dependent Inactivation. Neuron *101*, 1134–1149.e3.

Adams, D.J., Dwyer, T.M., and Hille, B. (1980). The permeability of endplate channels to monovalent and divalent metal cations. J. Gen. Physiol. *75*, 493–510.

Alawieyah Syed Mortadza, S., Sim, J.A., Neubrand, V.E., and Jiang, L.H. (2018). A critical role of TRPM2 channel in Aβ$_{42}$ -induced microglial activation and generation of tumor necrosis factor-α. Glia *66*, 562–575.

Autzen, H.E., Myasnikov, A.G., Campbell, M.G., Asarnow, D., Julius, D., and Cheng, Y. (2018). Structure of the human TRPM4 ion channel in a lipid nanodisc. Science *359*, 228–232.

Bernèche, S., and Roux, B. (2005). A gate in the selectivity filter of potassium channels. Structure *13*, 591–600.

Blenn, C., Wyrsch, P., Bader, J., Bollhalder, M., and Althaus, F.R. (2011). Poly(ADP-ribose)glycohydrolase is an upstream regulator of Ca2+ fluxes in oxidative cell death. Cell. Mol. Life Sci. *68*, 1455–1466.

Bo, X., Jiang, L.H., Wilson, H.L., Kim, M., Burnstock, G., Surprenant, A., and North, R.A. (2003). Pharmacological and biophysical properties of the human P2X5 receptor. Mol. Pharmacol. *63*, 1407–1416.

Coyle, J.T., and Puttfarcken, P. (1993). Oxidative stress, glutamate, and neurodegenerative disorders. Science *262*, 689–695.

Dietrich, A., and Gudermann, T. (2008). Another TRP to endothelial dysfunction: TRPM2 and endothelial permeability. Circ. Res. *102*, 275–277.

DiMaio, F., Song, Y., Li, X., Brunner, M.J., Xu, C., Conticello, V., Egelman, E., Marlovits, T., Cheng, Y., and Baker, D. (2015). Atomic-accuracy models from 4.5-Å cryo-electron microscopy data with density-guided iterative local refinement. Nat. Methods *12*, 361–365.

Diver, M.M., Cheng, Y., and Julius, D. (2019). Structural insights into TRPM8 inhibition and desensitization. Science *365*, 1434–1440.

Du, J., Xie, J., and Yue, L. (2009). Intracellular calcium activates TRPM2 and its alternative spliced isoforms. Proc. Natl. Acad. Sci. USA *106*, 7239–7244.

Dutzler, R., Campbell, E.B., and MacKinnon, R. (2003). Gating the selectivity filter in ClC chloride channels. Science *300*, 108–112.

Fliegert, R., Watt, J.M., Schöbel, A., Rozewitz, M.D., Moreau, C., Kirchberger, T., Thomas, M.P., Sick, W., Araujo, A.C., Harneit, A., et al. (2017). Ligand-induced activation of human TRPM2 requires the terminal ribose of ADPR and involves Arg1433 and Tyr1349. Biochem. J. *474*, 2159–2175.

Goehring, A., Lee, C.-H., Wang, K.H., Michel, J.C., Claxton, D.P., Baconguis, I., Althoff, T., Fischer, S., Garcia, K.C., and Gouaux, E. (2014). Screening and large-scale expression of membrane proteins in mammalian cells for structural studies. Nat. Protoc. *9*, 2574–2585.

Guo, J., She, J., Zeng, W., Chen, Q., Bai, X.C., and Jiang, Y. (2017). Structures of the calcium-activated, non-selective cation channel TRPM4. Nature *552*, 205–209.

Hara, Y., Wakamori, M., Ishii, M., Maeno, E., Nishida, M., Yoshida, T., Yamada, H., Shimizu, S., Mori, E., Kudoh, J., et al. (2002). LTRPC2 Ca2+-permeable channel activated by changes in redox status confers susceptibility to cell death. Mol. Cell *9*, 163–173.

Huang, Y., Winkler, P.A., Sun, W., Lü, W., and Du, J. (2018). Architecture of the TRPM2 channel and its activation mechanism by ADP-ribose and calcium. Nature *562*, 145–149.

Huang, Y., Roth, B., Lü, W., and Du, J. (2019). Ligand recognition and gating mechanism through three ligand-binding sites of human TRPM2 channel. eLife *8*, e50175.

Jara-Oseguera, A., Huffer, K.E., and Swartz, K.J. (2019). The ion selectivity filter is not an activation gate in TRPV1-3 channels. eLife *8*, e51212.

Jiang, L.H., Yang, W., Zou, J., and Beech, D.J. (2010). TRPM2 channel properties, functions and therapeutic potentials. Expert Opin. Ther. Targets *14*, 973–988.

Jiang, Q., Gao, Y., Wang, C., Tao, R., Wu, Y., Zhan, K., Liao, M., Lu, N., Lu, Y., Wilcox, C.S., et al. (2017). Nitration of TRPM2 as a Molecular Switch Induces Autophagy During Brain Pericyte Injury. Antioxid. Redox Signal. *27*, 1297–1316.

Julius, D. (2013). TRP channels and pain. Annu. Rev. Cell Dev. Biol. *29*, 355–384.

Kashio, M., Sokabe, T., Shintaku, K., Uematsu, T., Fukuta, N., Kobayashi, N., Mori, Y., and Tominaga, M. (2012). Redox signal-mediated sensitization of transient receptor potential melastatin 2 (TRPM2) to temperature affects macrophage functions. Proc. Natl. Acad. Sci. USA *109*, 6745–6750.

Kietzmann, T., Fandrey, J., and Acker, H. (2000). Oxygen Radicals as Messengers in Oxygen-Dependent Gene Expression. News Physiol. Sci. *15*, 202–208.

Ko, S.Y., Wang, S.E., Lee, H.K., Jo, S., Han, J., Lee, S.H., Choi, M., Jo, H.R., Seo, J.Y., Jung, S.J., and Son, H. (2019). Transient receptor potential melastatin 2 governs stress-induced depressive-like behaviors. Proc. Natl. Acad. Sci. USA *116*, 1770–1775.

Kopec, W., Rothberg, B.S., and de Groot, B.L. (2019). Molecular mechanism of a potassium channel gating through activation gate-selectivity filter coupling. Nat. Commun. *10*, 5366.

Kühn, F.J., and Lückhoff, A. (2004). Sites of the NUDT9-H domain critical for ADP-ribose activation of the cation channel TRPM2. J. Biol. Chem. *279*, 46431–46437.

Launay, P., Fleig, A., Perraud, A.L., Scharenberg, A.M., Penner, R., and Kinet, J.P. (2002). TRPM4 is a Ca2+-activated nonselective cation channel mediating cell membrane depolarization. Cell *109*, 397–407.

Leaver-Fay, A., Tyka, M., Lewis, S.M., Lange, O.F., Thompson, J., Jacak, R., Kaufman, K., Renfrew, P.D., Smith, C.A., Sheffler, W., et al. (2011). ROSETTA3: an object-oriented software suite for the simulation and design of macromolecules. Methods Enzymol. *487*, 545–574.

Li, M., Du, J., Jiang, J., Ratzan, W., Su, L.T., Runnels, L.W., and Yue, L. (2007). Molecular determinants of Mg2+ and Ca2+ permeability and pH sensitivity in TRPM6 and TRPM7. J. Biol. Chem. *282*, 25817–25830.

Liu, Y., Holmgren, M., Jurman, M.E., and Yellen, G. (1997). Gated access to the pore of a voltage-dependent K+ channel. Neuron *19*, 175–184.

Luo, Y., Yu, X., Ma, C., Luo, J., and Yang, W. (2018). Identification of a Novel EF-Loop in the N-terminus of TRPM2 Channel Involved in Calcium Sensitivity. Front. Pharmacol. *9*, 581.

Luo, Y.H., Yu, X.F., Ma, C., Yang, F., and Yang, W. (2019). Effects of calcium-binding sites in the S2-S3 loop on human and Nematostella vectensis TRPM2 channel gating processes. J. Zhejiang Univ. Sci. B *20*, 972–982.

Mandell, D.J., Coutsias, E.A., and Kortemme, T. (2009). Sub-angstrom accuracy in protein loop reconstruction by robotics-inspired conformational sampling. Nat. Methods *6*, 551–552.

Mastronarde, D.N. (2005). Automated electron microscope tomography using robust prediction of specimen movements. J. Struct. Biol. *152*, 36–51.

McKemy, D.D., Neuhausser, W.M., and Julius, D. (2002). Identification of a cold receptor reveals a general role for TRP channels in thermosensation. Nature *416*, 52–58.

Miller, B.A., Hoffman, N.E., Merali, S., Zhang, X.Q., Wang, J., Rajan, S., Shanmughapriya, S., Gao, E., Barrero, C.A., Mallilankaraman, K., et al. (2014). TRPM2 channels protect against cardiac ischemia-reperfusion injury: role of mitochondria. J. Biol. Chem. *289*, 7615–7629.

Nagamine, K., Kudoh, J., Minoshima, S., Kawasaki, K., Asakawa, S., Ito, F., and Shimizu, N. (1998). Molecular cloning of a novel putative Ca2+ channel protein (TRPC7) highly expressed in brain. Genomics *54*, 124–131.

Ostapchenko, V.G., Chen, M., Guzman, M.S., Xie, Y.F., Lavine, N., Fan, J., Beraldo, F.H., Martyn, A.C., Belrose, J.C., Mori, Y., et al. (2015). The Transient Receptor Potential Melastatin 2 (TRPM2) Channel Contributes to β-Amyloid Oligomer-Related Neurotoxicity and Memory Impairment. J. Neurosci. *35*, 15157–15169.

Owsianik, G., Talavera, K., Voets, T., and Nilius, B. (2006). Permeation and selectivity of TRP channels. Annu. Rev. Physiol. *68*, 685–717.

Perraud, A.L., Fleig, A., Dunn, C.A., Bagley, L.A., Launay, P., Schmitz, C., Stokes, A.J., Zhu, Q., Bessman, M.J., Penner, R., et al. (2001). ADP-ribose gating of the calcium-permeable LTRPC2 channel revealed by Nudix motif homology. Nature *411*, 595–599.

Perraud, A.L., Shen, B., Dunn, C.A., Rippe, K., Smith, M.K., Bessman, M.J., Stoddard, B.L., and Scharenberg, A.M. (2003). NUDT9, a member of the Nudix hydrolase family, is an evolutionarily conserved mitochondrial ADP-ribose pyrophosphatase. J. Biol. Chem. *278*, 1794–1801.

Pettersen, E.F., Goddard, T.D., Huang, C.C., Couch, G.S., Greenblatt, D.M., Meng, E.C., and Ferrin, T.E. (2004). UCSF Chimera—a visualization system for exploratory research and analysis. J. Comput. Chem. *25*, 1605–1612.

Pippel, A., Stolz, M., Woltersdorf, R., Kless, A., Schmalzing, G., and Markwardt, F. (2017). Localization of the gate and selectivity filter of the full-length P2X7 receptor. Proc. Natl. Acad. Sci. USA *114*, E2156–E2165.

Salazar, H., Jara-Oseguera, A., Hernández-García, E., Llorente, I., Arias-Olguín, I.I., Soriano-García, M., Islas, L.D., and Rosenbaum, T. (2009). Structural determinants of gating in the TRPV1 channel. Nat. Struct. Mol. Biol. *16*, 704–710.

Smart, O.S., Goodfellow, J.M., and Wallace, B.A. (1993). The pore dimensions of gramicidin A. Biophys. J. *65*, 2455–2460.

Tao, X., Hite, R.K., and MacKinnon, R. (2017). Cryo-EM structure of the open high-conductance Ca^{2+}-activated K$^+$ channel. Nature *541*, 46–51.

Tong, Q., Zhang, W., Conrad, K., Mostoller, K., Cheung, J.Y., Peterson, B.Z., and Miller, B.A. (2006). Regulation of the transient receptor potential channel TRPM2 by the Ca2+ sensor calmodulin. J. Biol. Chem. *281*, 9076–9085.

Tóth, B., and Csanády, L. (2012). Pore collapse underlies irreversible inactivation of TRPM2 cation channel currents. Proc. Natl. Acad. Sci. USA *109*, 13440–13445.

Uchida, K., and Tominaga, M. (2011). TRPM2 modulates insulin secretion in pancreatic β-cells. Islets *3*, 209–211.

Wang, C., Bradley, P., and Baker, D. (2007). Protein-protein docking with backbone flexibility. J. Mol. Biol. *373*, 503–519.

Wang, R.Y., Kudryashev, M., Li, X., Egelman, E.H., Basler, M., Cheng, Y., Baker, D., and DiMaio, F. (2015). De novo protein structure determination from near-atomic-resolution cryo-EM maps. Nat. Methods *12*, 335–338.

Wang, L., Fu, T.M., Zhou, Y., Xia, S., Greka, A., and Wu, H. (2018). Structures and gating mechanism of human TRPM2. Science *362*, eaav4809.

Xia, R., Mei, Z.Z., Mao, H.J., Yang, W., Dong, L., Bradley, H., Beech, D.J., and Jiang, L.H. (2008). Identification of pore residues engaged in determining divalent cationic permeation in transient receptor potential melastatin subtype channel 2. J. Biol. Chem. *283*, 27426–27432.

Yang, H., and Cui, J. (2015). BK channels. In Handbook of Ion Channels, J. Zheng and M.C. Trudeau, eds. (CRC Press), pp. 227–239.

Ye, M., Yang, W., Ainscough, J.F., Hu, X.P., Li, X., Sedo, A., Zhang, X.H., Zhang, X., Chen, Z., Li, X.M., et al. (2014). TRPM2 channel deficiency prevents delayed cytosolic Zn2+ accumulation and CA1 pyramidal neuronal death after transient global ischemia. Cell Death Dis. *5*, e1541.

Yin, Y., Wu, M., Hsu, A.L., Borschel, W.F., Borgnia, M.J., Lander, G.C., and Lee, S.Y. (2019). Visualizing structural transitions of ligand-dependent gating of the TRPM2 channel. Nat. Commun. *10*, 3740.

Yu, P., Xue, X., Zhang, J., Hu, X., Wu, Y., Jiang, L.H., Jin, H., Luo, J., Zhang, L., Liu, Z., and Yang, W. (2017). Identification of the ADPR binding pocket in the NUDT9 homology domain of TRPM2. J. Gen. Physiol. *149*, 219–235.

Yu, P., Liu, Z., Yu, X., Ye, P., Liu, H., Xue, X., Yang, L., Li, Z., Wu, Y., Fang, C., et al. (2019). Direct Gating of the TRPM2 Channel by cADPR via Specific Interactions with the ADPR Binding Pocket. Cell Rep. *27*, 3684–3695.e4.

Zhang, Z., Tóth, B., Szollosi, A., Chen, J., and Csanády, L. (2018). Structure of a TRPM2 channel in complex with Ca(2+) explains unique gating regulation. eLife *7*, e36409.

Zheng, J., and Sigworth, F.J. (1997). Selectivity changes during activation of mutant Shaker potassium channels. J. Gen. Physiol. *110*, 101–117.

Zheng, J., and Trudeau, M.C. (2015). Handbook of ion channels (CRC Press).

Zheng, S.Q., Palovcak, E., Armache, J.P., Verba, K.A., Cheng, Y., and Agard, D.A. (2017). MotionCor2: anisotropic correction of beam-induced motion for improved cryo-electron microscopy. Nat. Methods *14*, 331–332.

STAR★METHODS

KEY RESOURCES TABLE

REAGENT or RESOURCE	SOURCE	IDENTIFIER
Bacterial and virus strains		
DH10-Bac	GIBCO	Cat# 10359016
BL21(DE3)	Takara	Cat# 9126
Chemicals, peptides, and recombinant proteins		
FBS Premium	PAN	Cat# ST30-3302
FuGENE6 Transfection Reagent	Promega	Cat# E2691
Protease Inhibitor Cocktail, mini-Tablet	MCE	Cat# HY-K0011
TEV protease	Solarbio	Cat# P2060
SMM-293TI	SinoBiological	Cat# M293TI
SIM SF	SinoBiological	Cat# MSF1
Sodium Butyrate	Sigma	Cat# 303410
Tetracycline	BBI	Cat# A600504
Gentamycin	BBI	Cat# A100304
$AgNO_3$	Sigma	Cat# 31630
TCEP	Sigma	Cat# 32434
Lauryl Maltose Neopentyl Glycol (LMNG)	Anatrace	Cat# NG310
Cholesteryl Hemisuccinate Tris Salt (CHS)	Anatrace	Cat# CH210
GDN	Anatrace	Cat# GDN101
POPC	Anatrace	Cat# P516
POPE	Anatrace	Cat# P416
POPG	Anatrace	Cat# P616
Amylose resin	NEB	Cat# E8021S
Biobeads	Bio-Rad	Cat# 1528920
Critical commercial assays		
QIAprep Spin Miniprep Kit (50)	QIAGEN	Cat# 27104
Deposited data		
Apo hsTRPM2 in nanodisc (map)	This paper	EMDB: EMD-32082
Apo hsTRPM2 in nanodisc (model)	This paper	PDB:7VQ1
Apo hsTRPM2 TMD in nanodisc (map)	This paper	EMDB: EMD-32083
Apo hsTRPM2 TMD in nanodisc (model)	This paper	PDB:7VQ2
Experimental models: Cell lines		
HEK293T	ATCC	Cat# CRL-11268
HEK293F	Thermo fisher	Cat# R79007
SF9	Expression Systems	Cat# 94-001
Oligonucleotides		
See Table S2 for list of TRPM2 mutants primers	This paper	N/A
Recombinant DNA		
pcDNA3.1-hsTRPM2	The A.M.Scharenberg Lab	GeneBank: NP_003298.1
pcDNA3.1-nvTRPM2	This paper	GeneBank: XP_001622235.1
pEG-BacMam-MBP-human TRPM2	This paper	GeneBank: NP_003298.1
Software and algorithms		
Graph Pad Prism 6	N/A	https://www.graphpad.com/

Continued

REAGENT or RESOURCE	SOURCE	IDENTIFIER
Relion 3.0	N/A	https://www3.mrc-lmb.cam.ac.uk/relion/index.php?title=Main_Page
Igor 5.0	N/A	https://www.wavemetrics.com/
Rosetta Suite	N/A	https://www.rosettacommons.org/software
HOLE	N/A	http://www.holeprogram.org/
UCSF Chimera	N/A	https://www.cgl.ucsf.edu/chimera/
PyMOL	Schrödinger	https://pymol.org/2/
Coot	N/A	https://www2.mrc-lmb.cam.ac.uk/personal/pemsley/coot/binaries/
Other		
Quantifoil R 1.2/1.3 on 300 copper mesh	Quantifoil	Cat# Q3100CR1.3

RESOURCE AVAILABILITY

Lead contact

Further information and requests for resources and reagents should be directed to and will be fulfilled by the Lead Contact, Wei Yang (yangwei@zju.edu.cn).

Materials availability

Plasmids generated in this study will be shared by the lead contact upon request. This study did not generate new unique reagents.

Data and code availability

- Data reported in this paper will be shared by the lead contact upon request.
- Cryo-EM density maps have been deposited in the Electron Microscopy Data Bank (EMDB) under accession numbers EMD-32082 for ligand-free *hs*TRPM2 and EMD-32083 for the transmembrane domains of hsTRPM2. Structure coordinates have been deposited in the Protein Data Bank (PDB) under accession number 7VQ1 for the ligand-free *hs*TRPM2 and 7VQ2 for the transmembrane domains of hsTRPM2.
- Any additional information required to reanalyze the data reported in this paper is available from the lead contact upon request.

EXPERIMENTAL MODEL AND SUBJECT DETAILS

Cell lines

Spodoptera frugiperda 9 cells (Sf9) are generated from Expression Systems (Cat# 94-001), and Human Embryonic Kidney 293T and 293F cells (HEK293T and HEK293F) are purchased from ATCC and Thermo fisher, respectively. They are available from the lead contact upon request.

Human TRPM2 construct design

For structure determination, the full-length human TRPM2 gene sequence (gene: https://www.ncbi.nlm.nih.gov/gene, protein accession number: NP_003298.1) was subcloned into a modified pEG-BacMam vector containing a maltose-binding protein (MBP) tag linked by a tobacco etch virus (TEV) protease cleavage site (Wang et al., 2018). For function assay, this cDNA, as well as *nv*TRPM2 cDNA (GeneBank: XP_001622235.1), was subcloned into pcDNA3.1 vector reported previously (Luo et al., 2018, 2019; Yu et al., 2017, 2019). These TRPM2 constructs in this study will be shared by the lead contact upon request.

METHOD DETAILS

Cell culture

For structure determination. *Spodoptera frugiperda* 9 cells (Sf9) were kept at 27°C in an atmosphere without CO_2 and grown in SIM SF medium (Sino Biological Inc.) supplemented with 2% fetal bovine serum (vol/vol). Transfections were performed using FuGENE6 Transfection Reagent (Promega) for V0 generation. Human embryonic kidney 293F cells (HEK293F) were kept at 37°C in an atmosphere with 8% CO_2 and grown in SMM 293-TI medium (Sino Biological Inc.) supplemented with 2% fetal bovine serum (vol/vol). For electrophysiology assay, human embryonic kidney 293T cells (HEK293T) were purchased from ATCC (CRL-3216), kept at 37°C in an

atmosphere with 5% CO_2 and grown in Dulbecco's modified Eagle's medium (DMEM, GIBCO) supplemented with 10% fetal bovine serum (vol/vol). For transfection, cells were detached with trypsin, re-suspended in DMEM and seeded onto glass coverslips in 35-mm dishes at 10%–40% confluency. Transfections were performed on the second day using FuGENE6 Transfection Reagent (Promega). Plasmids expressing full-length human TRPM2 channel or mutants were co-transfected with pEGFP-N1 (Invitrogen) at a ratio of 2:1 to visualize successfully transfected cells. Electrophysiological recordings were done 24-48 h after transfection.

Expression and purification
The full-length human TRPM2 (*hs*TRPM2) construct was transformed into DH10Bac cells for bacmid production. The bacmid containing the TRPM2 gene was used to transfect Sf9 cells using FuGENE® HD Transfection Reagent (Promega) for baculovirus production. P2 virus was used to infect a suspension of HEK293F cells incubated at 37°C. Sodium butyrate (10 mM) was added to the suspension 20 h post-infection and the temperature was adjusted to 30°C to increase protein expression. Sixty hours after infection, cells were collected and washed with H buffer [150 mM NaCl, 40 mM HEPES, 2mM Tris (2-carboxyethyl) phosphine hydrochloride (TCEP), pH 8.0]. After collection, cells were lysed in H buffer containing 2 mM pepstatin, 0.8 μM aprotinin, 2 μg ml^{-1} leupeptin and 1 mM phenylmethylsulfonyl fluoride (PMSF). After lysis, Lauryl Maltose Neopentyl Glycol (LMNG) and cholesteryl hemisuccinate (CHS) were added to give a final concentration of 1% and 0.1% respectively. After solubilization for 1 h, cell debris was removed by centrifugation at 17,000 *rpm* (JA-25.50 Fixed-Angle Rotor, Beckman Coulter, Inc.) for 40 minutes. The supernatant was incubated with Amylose resin (New England BioLabs) for 2 h and then washed with ten bed volumes of wash buffer [H buffer containing 0.05% glyco-diosgenin (GDN)]. The protein was eluted with elute buffer (H buffer containing 0.05% GDN, 10 mM maltose). The eluent components were concentrated in an Amicon ultra-15 centrifugal filter (100 kD cut-off, Millipore), followed by overnight incubation with TEV protease (Sigma-Aldrich) to remove the MBP tag. The protein was ultracentrifuged using a 45 Ti rotor at 186,000 *g* for 40 min at 4°C (Beckman Coulter, Inc.) and loaded onto a Superose 6 column (GE Healthcare) pre-equilibrated with GF buffer (H buffer containing 0.05% GDN).

The peak fractions were collected and concentrated to 1 mg/mL using a centrifugal filter (100 kD cut-off, Millipore) and to reconstituted into lipid nanodisc following the published protocol (Guo et al., 2017). Briefly, *hs*TRPM2, MSP1 (Goehring et al., 2014) and lipids (POPC: POPE: POPG = 3:1:1) were mixed at a molar ratio of 1:8:10, and incubated on ice for 30 minutes. Detergents were removed by additional Bio-Beads SM2 (Bio-Rad) to a concentration of 80 mg/mL followed by gentle agitation. The used Bio-Beads were replaced with fresh ones every 4 h, and totally 2 times. Then, the sample was collected and further centrifuged at 100,000 *g* for 30 minutes. The supernatant was loaded onto a Superose 6 Increase 10/300 GL column pre-equilibrated with H buffer. The peak fraction for tetramer-*hs*TRPM2 was collected for Coomassie Brilliant Blue (CBB) staining check and cryo-EM determination (Figure S1A).

Electron microscopy sample preparation and data acquisition
*hs*TRPM2 nanodisc was concentrated to 1.5 mg/mL in H buffer before freezing. The samples were prepared via Thermo Fisher Vitrobot Mk IV at 4°C and 100% humidity. A sample volume of 3 μL was applied to a freshly glow-discharged Quantiofoil R 1.2/1.3 300-mesh Cu holey carbon grids, blotted with filter paper for 3 s with a 5 s wait time and 2 s drain time followed by plunge-freezing in liquid-ethane cooled by liquid nitrogen.

TRPM2 dataset was collected using a Titan Krios (Thermo Fisher) transmission electron microscope operating at 300 kV equipped with a Gatan K3 Summit direct electon detector in super resolution mode (binned pixel size of 0.855 Å). Each movie contains 32 frames with a total exposure time of 2 s, resulting a total accumulated dose of ~60 e/Å^2. The images were recorded using the automated acquisition program SerialEM (Mastronarde, 2005) with nominal defocus ranges from −0.8 to −1.6 μm.

Electron microscopy data processing
A total of 5,535 movies were acquired and used for data processing. Motion correction and dose weighting were performed using MotionCor2, followed by CTF estimation of unweighted summed images using Gctf in RELION-3.0 (Zheng et al., 2017). Difference of Gaussians (DoG) picker was used to automatically pick the entire dataset (1,541,101 particles). After 2D classification, a set of particles from one class (262,104 particles) which showed clear transmembrane and cytoplasmic domains was recentered, reextracted, and subjected to 3D auto-refinement with C4 symmetry with a soft mask surrounding the full density, yielding a final reconstruction of ~3.7 Å, as estimated by the gold-standard 0.143 Fourier shell correlation (FSC) (Figures S1A and S1B).

For further determination of TMD structure of ligand free state, we first generated a soft mask covering the transmembrane domain of the channel and used the particle subtraction function in Relion to subtract the density outside these regions from the raw particles. Later, 3D refinement was used to align these "subtracted particles" based the remaining density, which resulted in a 3.68 Å Map (Figure S1B).

Computational modeling
Loop modeling of the selectivity filter of the TRPM2 channel in Apo state was performed using the Rosetta Suite (Leaver-Fay et al., 2011). TRPM2 channel structure (PDB ID: 6PUR) was used as a template. The loop regions of selectivity filter domain in each subunit of the tetramer were modeled *de novo*. During the first round of modeling, Rosetta's cyclic coordinate descent (CCD) loop relax protocol (Wang et al., 2007) was used and the top 10 cluster center models were passed to the second round. During the second to sixth

rounds of modeling, kinematic loop relax protocol (KIC) (Mandell et al., 2009) was used and the top 10 cluster center models were passed to the next round. During the rest rounds of modeling, kinematic loop relax protocol was used and the top 10 models by score were passed to the next round. From 5,000 to 10,000 models were generated in each round. The models shown here represent the 10 lowest energy models from the last round of iterative loop relax. Loop modeling of S5-S6 linker was performed using kinematic loop relax protocol (KIC).

Electron density map was used as constraints in each round. We set the elec_dens_fast weight to 65.0 according to the density map resolution, starting model quality, and protocol (DiMaio et al., 2015; Wang et al., 2015). The resolution of the map was set to 3.7 Å. Maps were also be resampled to reduce memory usage and runtime. The grid sampling of the map was set to 1.8. Pore radius of the TRPM2 model was calculated by the HOLE program version 2.0 (Smart et al., 1993). All molecular graphics of TRPM2 models were rendered by UCSF Chimera software version 1.13 (Pettersen et al., 2004).

Electrophysiology

Whole-cell current recordings were performed using a HEKA EPC10 amplifier at room temperature as described previously (Yu et al., 2019). Specifically (except for Ag^+-modification assay), the extracellular solution contained W-Na-ECS (150 mM NaCl, 2 mM $CaCl_2$, 10 mM HEPES, and 13 mM glucose, pH 7.4) and W-Ca-ECS (110 mM $CaCl_2$, 10 mM HEPES, and 13 mM glucose, pH 7.4). The intracellular solution (W-K-ICS) contained 150 mM KCl, 0.05 mM EGTA, 10 mM HEPES, and ADPR at indicated concentrations (500 μM), pH 7.3. For whole cell recording in symmetric Na^+ solution, the 150 mM KCl in W-K-ICS was replaced by 150 mM NaCl and named W-Na-ICS. The membrane potential was held at 0 mV, and a voltage ramp of 500 ms duration from −100 mV to 100 mV was applied every 5 s. Glass pipettes with a resistance of 3-5 MΩ were used. Data were acquired at 10 kHz and filtered offline during data analysis. Change of the extracellular solution was performed using a RSC-200 system (Bio-Logic Science Instruments).

The reversal or zero-current potential (E_r) was determined from current responses to the aforementioned voltage ramps under a potassium intracellular solution (W-K-ICS) and sodium or calcium extracellular solution (W-Na-ECS or W-Ca-ECS). The single channel conductance was calculated by followed equation.

$$G_{SC} = I_{SC} * 1,000 / (V_{holding} - V_{rev}) \tag{Equation 1}$$

where the G_{sc} and I_{sc} are the single channel conductance and single channel current respectively. $V_{holding}$ is the membrane holding potential, V_{rev} is the reversal potential.

After cell-attached configuration was established in extracellular solution (W-Na-ECS, W-Ca-ECS), application of voltage ramps started and continued throughout experiments. To determinate the reversal potentials of Ca^{2+} (E_{r-Ca}), the whole-cell configuration was achieved at least 2 min after W-Na-ECS was replaced with W-Ca-ECS. The N-(p-amylcinnamoyl) anthranilic acid (ACA) -insensitive current components were negligible, and no subtraction from the total currents was made. The reversal potentials were corrected for liquid junction potentials as we described previously (Bo et al., 2003). Ion activities were used, converted from ion concentrations using the following coefficients: $\gamma Na^+ = 0.75$, $\gamma Ca^{2+} = 0.28$.

$$[Na^+]_{bath} = [Na^+]_{ECS} * \gamma Na^+ \tag{Equation 2}$$

$$[Ca^{2+}]_{bath} = [Ca^{2+}]_{ECS} * \gamma Ca^{2+} \tag{Equation 3}$$

The relative permeability P_X/P_K (X = Ca^{2+}, Na^+ or K^+) were derived using the Goldman-Hodgkin-Katz equation (Li et al., 2007; Perraud et al., 2001):

$$PNa^+ / PK^+ = [Na^+]_{bath} / [K^+]_{pipette} V_{rev} F / RT \tag{Equation 4}$$

$$PCa^{2+} / PK^+ = ([K^+]_{pipette} V_{rev} F / RT (1 + e^{V_{rev} F / RT})) / 4 [Ca^{2+}]_{bath} \tag{Equation 5}$$

$$PCa^{2+} / PNa^+ = [PCa^{2+} / PK^+] / [PNa^+ / PK^+] \tag{Equation 6}$$

Where F, R, and T are Faraday constant, gas constant, and absolute temperature (Adams et al., 1980; Guo et al., 2017; Owsianik et al., 2006; Xia et al., 2008).

Single channel recordings were performed using a HEKA EPC10 amplifier controlled with PatchMaster software (HEKA). The membrane potential was held at −80 mV and currents were recorded by the gap-free protocol with coapplying ADP-ribose and Ca^{2+} to the cytoplasmic side. Glass pipettes with a resistance of 6-7 MΩ were used. The intracellular solution (S-K-ICS) contained 150 mM KCl, 10 μM $CaCl_2$, 10 mM HEPES, and 100 μM ADPR, pH 7.3. The extracellular solution contained W-Na-ECS (150 mM NaCl, 2 mM $CaCl_2$, 10 mM HEPES, and 13 mM glucose, pH 7.4) and W-Ca-ECS (110 mM $CaCl_2$, 10 mM HEPES, and 13 mM glucose, pH 7.4). Data were filtered at 2.25 kHz and sampled at 12.5 kHz. Change of the intracellular solution was performed using a RSC-200 system (Bio-Logic

Science Instruments). Single-channel data was processed by the Igor Pro software version 5. Opening and closing events were detected during idealization with the half amplitude method.

Ag⁺-modification assay

AgNO$_3$ (S8157, Sigma Aldrich) stock solutions were prepared freshly in water, first at 100 mM and then further diluted to 1 mM, freshly used at a concentration of 10 μM diluted in extracellular solutions 1:100 dilution. Under our experimental conditions, a total of 10 μM AgNO$_3$ was calculated to yield 100 nM free Ag⁺ using MaxChelator Software. All Ag⁺-containing solutions were covered in aluminum foil to protect them from light, as well as the solution container in the perfusion system, and all the solutions were used (Salazar et al., 2009).

Whole-cell current recordings were performed by using a HEKA EPC10 amplifier at room temperature as described previously. For Ag⁺-modification assay, all chloride in extracellular solution is replaced by nitrate. The extracellular solution contained Ag-Na-ECS [150 mM NaNO$_3$, 2 mM Ca(NO$_3$)$_2$, 10 mM HEPES, and 13 mM glucose, pH 7.4]. The pH was adjusted by NaOH (3M). The intracellular solution (W-K-ICS) contained 150 mM KCl, 0.05 mM EGTA, 10 mM HEPES, and ADPR at indicated concentrations (500 μM), pH 7.3. The specific operation flows between *hs*TRPM2 and *nv*TRPM2 channel are different.

hsTRPM2 Ag⁺ modification procedures

The experimental procedures are illustrated in Figure 5A. For bath state, the cells were pre-incubated in Ag-Na-ECS (100 nM Ag⁺ added) for 120 s after forming giga-seals and then washed by Ag-Free-Na-ECS (Ag⁺ free) for 30 s, after which the whole cell configuration was established for more than 2.5 min in Ag-Free-Na-ECS (Ag⁺ free) solution. For pre-incubation state, the cells were pre-incubated in Ag-Na-ECS for 120 s after forming giga-seals and then washed by Ag-Free-Na-ECS for 30 s, after which the whole cell configuration was established. Cells were perfused with Ag⁺ (Ag-Na-ECS) for 150 s when ADPR-induced currents reached steady state. For open state, cells were perfused by Ag-Free-Na-ECS (Ag⁺ free) solution. Ag⁺ (Ag-Na-ECS) was perfused for 150 s when getting the steady-state currents in ADPR, established by whole cell configuration. The membrane potential was held at 0 mV, and a voltage ramp of 500 ms duration from −100 mV to 100 mV was applied every 5 s.

To quantify the irreversible component of Ag⁺-inhibition, we plotted the steady-state ADPR-induced currents before Ag⁺-application for each trace in pre-incubation and open state (black arrows in Figures 5B, 5E, 5G, 5I, and S6L–S6O). t = 0 was set at the first sweep with Ag⁺-exposure, and was used to normalize each of the curves in the figure. The six data points correspond to the current values from the first recorded traces with exposure to Ag⁺ at 0 s, 10 s, 50 s, 100 s, 140 s, 150 s.

To evaluate the effect of Ag⁺-modification in pre-incubation and open states, we measured initial steady-state ADPR-induced currents in the presence of 100 nM Ag⁺ (set as t = 0) together with several exposure times (10 s, 50 s, 100 s, 140 s, 150 s). As control, we measured the currents at the same time point as before (pre-incubation state and open state) and calculated the value of I/I_{max} (defined as F_i) (I, current obtained after Ag⁺ treatment; I_{max}, current obtained at t = 0 with 500 μM ADPR and 100 nM Ag⁺).

$$F_i = I/I_{max} \qquad \text{(Equation 7)}$$

On the other hand, the time-courses for Ag⁺-modification in different states were fitted by mono-exponential function, to derive the time constant (τ). To further evaluate the effects of Ag⁺-modification, we also calculated the Ag⁺-modification rate (K_m) based on the time constant (τ) and the concentration of free Ag⁺ ($c_{Ag}{}^+$).

$$K_m = 1/(Tc_{Ag}{}^+) \qquad \text{(Equation 8)}$$

To evaluate whether Ag⁺-modification is reversible, we measured the currents of last sweep of Ag⁺-modification and Ag-Free-Na-ECS wash respectively in both pre-incubation state and open state, and calculated the value of I_{wash}/I_{Ag+} (defined as F_a) (I_{wash}, the current of last sweep of Ag-Free-Na-ECS wash; I_{Ag+}, the current of last sweep of Ag⁺ treatment).

$$F_a = I_{wash}/I_{Ag+} \qquad \text{(Equation 9)}$$

nvTRPM2 Ag⁺-modification procedures

The experimental procedures are illustrated in Figure 6A. The *nv*TRPM2 channel exhibits rapid inactivation, and so ADPR-evoked currents were recorded by gap-free protocol at −60 mV while for *hs*TRPM2, the voltage ramp protocol was used.

For bath state, the cells formed giga-seals and the whole cell configuration was established under Ag-Free-Na-ECS (Ag⁺ free) solution. For pre-incubation state, the cells were pre-incubated in Ag-Na-ECS (100 nM Ag⁺ added) for 120 s after forming giga-seals and then washed by Ag-Free-Na-ECS (Ag⁺ free) for 30 s, after which the whole cell configuration was established. For open state, the cells were perfused by Ag-Free-Na-ECS (Ag⁺ free) solution. Ag⁺ (Ag-Na-ECS) was perfused when establishing whole cell configuration. The membrane potential was held at −60 mV. The time required to reach the 10% of peak current was calculated as the delay time.

The time-courses for Ag⁺-modification (pre-incubation and open states) or not (bath state) were fitted by mono-exponential function, and the activation time constant (τ_a) and inactivation time constant (τ_i) were finally calculated. To further evaluate the effect of Ag⁺-modification, we also calculate the Ag⁺-modification rate (K_m) based on the activation time constant (τ_a) or inactivation time constant (τ_i) and $c_{Ag}{}^+$ (the concentration of free Ag⁺).

$$K_m = 1/(TC_{Ag}^+) \quad T = T_a \text{ or } T_i \qquad \text{(Equation 10)}$$

QUANTIFICATION AND STATISTICAL ANALYSIS

Data were analyzed with PatchMaster (HEKA) and Igor Pro 5 (Wave-Metrics). All results, where appropriate, are presented as mean ± SEM. Curve fitting (nonlinear regression) was performed using Prism7.0 software by single exponential (one phase decay) and singe channel conductance analysis using Igor Pro 5 (Wave-Metrics). Statistical comparisons were made by using one-way ANOVA with Bonferroni correction. $*p < 0.05$, $**p < 0.01$, $***p < 0.001$, $****p < 0.0001$ indicated statistical significance.